Phase-field simulations of velocity selection in rapidly solidified binary alloys

Jun Fan,[1] Michael Greenwood,[1] Mikko Haataja,[2] and Nikolas Provatas[1]
[1]*Department of Materials Science and Engineering and Brockhouse Institute for Materials Research, McMaster University, 1280 Main Street West, Hamilton, Ontario, Canada L8S 4L7*
[2]*Department of Mechanical and Aerospace Engineering and the Princeton Institute for the Science and Technology of Materials (PRISM), Princeton University, Princeton, New Jersey 08544, USA*
(Received 11 April 2006; revised manuscript received 13 June 2006; published 12 September 2006)

Time-dependent simulations of two-dimensional isothermal Ni-Cu dendrites are simulated using a phase-field model solved with a finite-difference adaptive mesh refinement technique. Dendrite tip velocity selection is examined and found to exhibit a transition between two markedly different regimes as undercooling is increased. At low undercooling, the dendrite tip growth rate is consistent with the kinetics of the classical Stefan problem, where the interface is assume to be in local equilibrium. At high undercooling, the growth velocity selected approaches a linear dependence on melt undercooling, consistent with the continuous growth kinetics of Aziz *et al.* and with a one-dimensional steady-state phase-field asymptotic analysis of Ahmad *et al.* [Phys. Rev. E **58**, 3436 (1998)]. Our simulations are also consistent with other previously observed behaviors of dendritic growth as undercooling is increased. These include the transition of dendritic morphology to absolute stability and nonequilibrium solute partitioning. Our results show that phase-field models of solidification, which inherently contain a nonzero interface width, can be used to study the dynamics of complex solidification phenomena involving both equilibrium and nonequilibrium interface growth kinetics.

DOI: 10.1103/PhysRevE.74.031602 PACS number(s): 68.70.+w, 81.30.Fb, 64.70.Dv, 82.20.Wt

I. INTRODUCTION

Rapid solidification plays an important role in the casting of technologically relevant alloys through the development of metastable phases and highly refined microstructures that exhibit very high-strength properties. While many properties of solidification microstructures at low to moderate cooling rates are fairly well understood, solidification growth rates and microstructure selection at high cooling rates, where nonequilibrium effects at the growth front dominate, remain unclear.

At low undercooling, the kinetics of solidification are governed by the classical Stefan problem, wherein the interface is assumed to be in local equilibrium. This describes solute (or heat for pure materials) diffusion in the bulk solid and liquid phases in conjunction with two kinetic boundary conditions at the solid-liquid interface: (1) the Gibbs-Thomson condition and (2) flux conservation across the solid-liquid interface. In the case of symmetric diffusion constants, the standard sharp-interface model (more precisely, a dimensionless form that is suitable to both alloy and pure dendrites) has been studied extensively [1–4], yielding predictions of dendritic tip growth rates and tip radius versus undercooling and surface tension anisotropy. These predictions were later separately confirmed with two-dimensional (2D) and three-dimensional (3D) phase-field simulations operating in the standard sharp-interface limit [5–7], and with experiments on nickel dendrites [7].

At high undercooling, on the other hand, experiments [8–11] and theoretical considerations [12–18] show that solidification kinetics differ markedly from those at low undercooling. In this regime, alloy solidification kinetics are expected to be dominated by nonequilibrium solute partitioning [12,19] and thermal effects [17,18]. More specifically, as the solidification rate increases, the length over which solute is diffused becomes comparable to the nanoscale interface separating the solid-liquid interface, making equilibrium solute redistribution into the liquid impossible ("solute trapping"). This limit is characterized by a mismatch in the chemical potential across the solid-liquid interface and a velocity-dependent local liquidus slope and solute partition coefficient. To date, there has not been a fully *self-consistent* solution of a sharp-interface solidification model valid in the high-undercooling regime (e.g., the continuous-growth model of Aziz *et al.* [16] or the nonequilibrium model Refs. [17,18], which also incorporate thermal effects). Some semi-empirical treatments usually treat the velocity as an input parameter from experiments [10] at high undercooling. Moreover, they do not produce independent predictions of both dendrite growth rate selection and morphology. Other models, which use marginal stability to obtain self-consistent predictions of tip velocity and radius [17,18], differ in significantly in their formulation from previous continuous growth models. Moreover, it is not expected that the predictions of these analytical approaches will be correct at low undercooling, where it is known that the predictions of marginal stability theory do not agree with those of solvability theory.

Simulating solidification microstructure evolution using sharp-interface models is usually a nontrivial task in 2D and 3D. Phase-field models of solidification offer a significantly simpler alternative. They are also physically based, derivable (in many cases) from a phenomenological free energy that makes contact with thermodynamic and microscopic properties of solidification [7]. For low undercooling, recent advances in phase-field matched asymptotics—a mathematical procedure for mapping the asymptotic behaviour of a phase-field model onto that of a sharp-interface model—provide several ways to quantitatively simulate the standard sharp-interface limit for the case of strongly asymmetric solute mobility, even with relatively diffuse interface widths

[20–22]. At high solidification velocities, 1D steady-state analysis [23], and 2D time-dependent thin-interface asymptotic analysis [24] both show that solidification phase-field models asymptotically map, to lowest order, onto a sharp-interface model containing the same physics as the continuous-growth model of Ref. [16]. Higher-order matched asymptotic analysis of solidification phase-field models further reveals that in the thin-interface limit, the flux conservation boundary condition should also contain an additional lateral surface diffusion term that scales with the interface width [21,22].

The objective of this paper is to investigate dendritic velocity and microstructure selection in rapidly solidified Ni-Cu alloys using two-dimensional, time-dependent phase-field simulations. Specifically, we wish to demonstrate that both equilibrium and nonequilibrium interface kinetics, and the associated change in velocity selection that they induce, can be captured in a unified and self-consistent way by the use of a phase-field model. The remainder of the paper is organized as follows. Section II introduces the phase-field model we employ, as well as a finite-difference adaptive mesh refinement algorithm. Section III discusses the transition to absolute stability of dendritic morphology as the undercooling is increased. In Sec. IV, we examine a corresponding transition in the dendritic growth velocity as undercooling is increased. In Sec. V, we examine that our simulations are consistent with the solute partitioning model of Aziz and co-workers [15,16].

II. 2D PHASE-FIELD MODEL AND NUMERICAL ALGORITHM

A. Phase-field model of solidification

In this work, we simulate isothermal solidification of a 2D binary alloy using the phase-field model of Ref. [23], which is expressed in dimensionless form by

$$\frac{1}{M_1}\frac{\partial \phi}{\partial t} = \vec{\nabla}\cdot(\epsilon^2(\theta)\vec{\nabla}\phi) - \frac{\partial}{\partial x}\left(\epsilon(\theta)\frac{d\epsilon(\theta)}{d\theta}\frac{\partial \phi}{\partial y}\right) + \frac{\partial}{\partial y}\left(\epsilon(\theta)\frac{d\epsilon(\theta)}{d\theta}\frac{\partial \phi}{\partial x}\right) - \frac{\partial f(\phi,C,T)}{\partial \phi} \tag{1}$$

$$\frac{\partial C}{\partial t} = \vec{\nabla}\cdot\left(M_2 C(1-C)\vec{\nabla}\frac{\partial f(\phi,C,T)}{\partial C}\right) \tag{2}$$

where ϕ is the phase-field parameter, which is taken as 0 in the liquid phase and 1 in the solid phase. The field $C(\vec{x},t)$ is the dimensionless (molar fraction) alloy concentration field, while T denotes the constant temperature. The parameter M_1 is related to the interface kinetic coefficient $\tilde{\mu}_A$ (see below), while M_2 is related to the solute diffusivity D (see below). The variable $\theta=\arctan\left(\frac{\partial\phi}{\partial y}/\frac{\partial\phi}{\partial x}\right)$ is the angle between the interface normal direction and x axis, while $\epsilon(\theta)=\epsilon_0[1+\epsilon_4\cos(\theta)]$ is the standard fourfold anisotropy function, with ϵ_0 related to the interface width l_A and the surface tension σ (see below). The function $f(\phi,C,T)$ is the bulk free-energy density

$$f(\phi,C,T) = Cf_B(\phi,T) + (1-C)f_A(\phi,T) + \frac{RT}{V_M}[C\ln C + (1-C)\ln(1-C)] \tag{3}$$

where $f_j(\phi,T)$ $(j=A,B)$ is the free-energy density of pure material A or B and V_M is the molar volume of the bulk material (assuming it is the same for A and B materials). R is the gas constant. The functions f_j are given by

$$f_j(\phi,T) = \frac{W_j}{4}g(\phi) + \frac{L_j(T-T_M^j)}{T_M^j}p(\phi) \tag{4}$$

where $W_j=12\sigma_j/l_j$, with l_j representing the interface width of material j and σ_j its surface tension energy. The parameters T_M^j and L_j represent the melting temperature and latent heat of fusion of material j, respectively. The interface interpolation functions $g(\phi)$ and $p(\phi)$ are given by

$$p(\phi) = \phi^2(3-2\phi), \quad g(\phi) = \phi^2(1-\phi)^2. \tag{5}$$

In what follows, we will assume that $\sigma_j=\sigma$ and $l_j=l$ for both materials A and B. The relation between the phase-field and materials parameters is then given by [23]

$$M_1 = \frac{\tilde{\mu}_A T_M^A}{6L_A l_A}, \quad M_2 = \frac{D(\phi)V_M}{RT}, \tag{6}$$

$$\epsilon_0^2 = 6\sigma l. \tag{7}$$

In the above model, time is measured in units of $\tau = 2L_A l_A^2/(\tilde{\mu}_A \sigma T_M^A)$ and space in units of $w=\sqrt{2}l_A$. The form of interpolation functions $D(\phi)$ is not known within the region of the solid-liquid interface. We approximate it in this work by a linear interpolation between the solid and liquid diffusivities $D(\phi)=D_S\phi+D_L(1-\phi)$ [23], where D_S and D_L are the solute diffusion coefficients of the solid and liquid phase, respectively. For the particular choices of $D(\phi)$, $p(\phi)$, $g(\phi)$ given above the phase-field model recovers, at high undercooling and within the limits of a 1D steady-state analysis, the kinetics of a particular continuous growth model of Refs. [16,23]. We note that by choosing the interpolation function $D(\phi)$, and the definition of the solid-liquid interface, it is possible to recover any particular continuous growth model in the thin-interface limit of Eqs. (1) and (2) [22]. The procedure to do this will be reported in a future presentation.

The phase-field model defined in Eqs. (1) and (2) was employed to investigate the growth rate and morphology selection by varying the nominal undercooling in Ni-Cu alloys. The material parameters used in the simulations are summarized in Table I. For computational expedience our simulations were run with varied sizes of the interface width (l_A^{eff}), which is artificially increased from the real value (l_A) by factors of 5, 10, 20, 40, and 100. For each value of the interface width, an effective liquid diffusion coefficient (D_L^{eff}) was introduced such that $D_L^{\text{eff}}/l_A^{\text{eff}}=D_L/l_A$. This allowed us to examine the effect of decreasing interface widths while maintaining an approximately invariant transition velocity scale separating the low- and high-undercooling regimes discussed below [see Eq. (10) below or Ref. [23]].

TABLE I. Materials parameters for the Ni-Cu system, reprinted from Ref. [23].

L_A	2.35×10^9 J/m^3
L_B	1.725×10^9 J/m^3
T_M^A	1728 K
T_M^B	1358 K
σ_A	0.28 J/m^2
σ_B	0.28 J/m^2
$\tilde{\mu}_A$	2.428 m/s K
D_L	10^{-9} m^2/s
D_S	10^{-14} m^2/s
l_A	6.48×10^{-10} m
l_B	6.48×10^{-10} m

B. Adaptive mesh refinement algorithm

The phase-field model was solved using a C++ adaptive mesh refinement (AMR) algorithm that uses finite differences to solve Eqs. (1) and (2). We have found that adaptation with finite differences allows approximately a 5–10 fold increase in simulation speed (measured as CPU time per node) over previous finite-element formulations [6,22,25], and an even further improvement of simulation efficiency for models containing higher-order spatial gradients (e.g., phase-field models of eutectic growth, or recent phase-field crystal models for pure materials [26] and alloys [27] solved in phase-amplitude space [24]).

Our finite-difference adaptive mesh refinement method stores nodes, rather than elements, on a data structure analogous to quad-tree structure. On a separate data structure, we also introduce so-called ghost nodes, which are used to carry out the appropriate finite differences at all simulation nodes. Ghosts nodes have their field values interpolated from nearby real nodes using standard bilinear interpolation. As in the finite-element AMR method we can determine the local refinement of the nodes by an error estimation from local gradients in the element, $\epsilon=C_1|\vec{\nabla}\phi|+C_2|\vec{\nabla}C|$, where C_1 and C_2 are constants. The code itself allows the user to substitute this criterion with any other error estimation scheme.

The use of an adaptive mesh allowed us to simulate systems sizes of $6400w\times6400w$, with a resolution of $dx=0.4w$ at the solid-liquid interface and a time step of $dt=0.01\tau$ in the simulation of Fig. 1(a) and $dt=0.0005\tau$ for Fig. 1(b). On a uniform mesh, such a system would require 256×10^6 nodes at all times, whereas at early times the AMR algorithm contains only a few thousand nodes. At late times, the efficiency of our algorithm scales with the available microstructure interface, not the system area (2D) or volume (3D). The basic reason for the improved performance of our AMR algorithm relies on the reduced number of operations per node required for one finite-difference update at a node, versus the number required using the finite-element method (FEM). Further details of the algorithm will be presented elsewhere. We note that our approach has many similarities with a finite-volume approach recently introduced in [28]. The efficiency of the finite-volume algorithm introduced in that work was reported to be similar to that of our previous FEM algorithm.

III. MORPHOLOGICAL TRANSITION OF THE GROWTH FRONT

Figure 1(a) shows a steady-state crystal morphology obtained at dimensionless nominal supersaturation, $\Omega=(C_L^{eq}-C_\infty)/(C_L^{eq}-C_S^{eq})=0.73$, where C_L^{eq} and C_S^{eq} denote the equilibrium solute concentrations in the liquid and solid phases, respectively, and C_∞ denotes the initial alloy composition (set in this work to $C_\infty=0.0717$). We note that the supersaturation measured the degree of undercooling below the liquidus line for a given average solute concentration C_∞. Specifically, the undercooling ΔT is related to the supersaturation with the following equality: $\Delta T=mC_\infty\Omega(1-k_e)/[1-\Omega(1-k_e)]$, where m is the absolute value of the liquidus slope, and k_e denotes the equilibrium partition coefficient. We note that as supersaturation increases, so too does the undercooling. We also note that the effective supersaturation at the interface deviates from Ω at high solidification rates, since it is calculated using the initial alloy concentration and the corresponding equilibrium solid and liquid concentrations; in fact, at high supersaturation, $\Omega=(C_L-C_\infty)/(C_L-C_S)\rightarrow1$,where C_L and C_S denote the nonequilibrium concentrations on the liquid and solid sides of the interface, respectively. The data was obtained for the case where $l_A^{eff}=100l_A=6.48\times10^{-8}$ m. As supersaturation is increased, fourfold-anisotropic crystals give way to a uniform nondendritic crystal morphology [Fig. 1(b), $\Omega=0.85$]. We note that since simulation time increases sharply as $l_A^{eff}\rightarrow l_A$ and $\Omega\rightarrow0$, we do not obtain truly steady-state dendritic structures at low supersaturation for the values of l_A we used in this work. At large Ω, however, we can observe uniform steady-state morphologies for all values of l_A^{eff}.

The morphological transition shown in Fig. 1 is caused by the transition of the interface to absolute stability. It has been observed in experiments [8,29,30] and has been simulated in previous phase-field studies [31,32]. This transition is characterized by a transition of dendritic structures, prevalent at low undercooling, to uniform or "globular" [32] structures at high undercooling.

Our phase-field simulations are consistent with theoretical arguments [33], which set a lower limit of absolute stability on the interface velocity $v_A=L\Delta TD/(k\sigma T_M^A)$ denoting the absolute stability velocity. This limit expresses the condition where the solute diffusion length becomes of the same order as the capillary length. We note that due to solute trapping effects, the partition coefficient becomes velocity dependent (see below), thus making the absolute stability velocity occur at lower value than predicted assuming equilibrium partitioning [31].

We also expect that for sufficiently large undercooling, the transition to complete solute trapping will render our morphological results invalid, as heat transfer becomes more important than mass transfer. Specifically, as the thermal diffusion length approaches the length scale of the crystal, the kinetics of the growing dendrite will thus be described by those of pure material with a modified melting temperature, with interface kinetics and curvature controlling the pattern selection process. To properly capture the onset of dendritic branching at very high undercooling we must thus include temperature variation in our model [34].

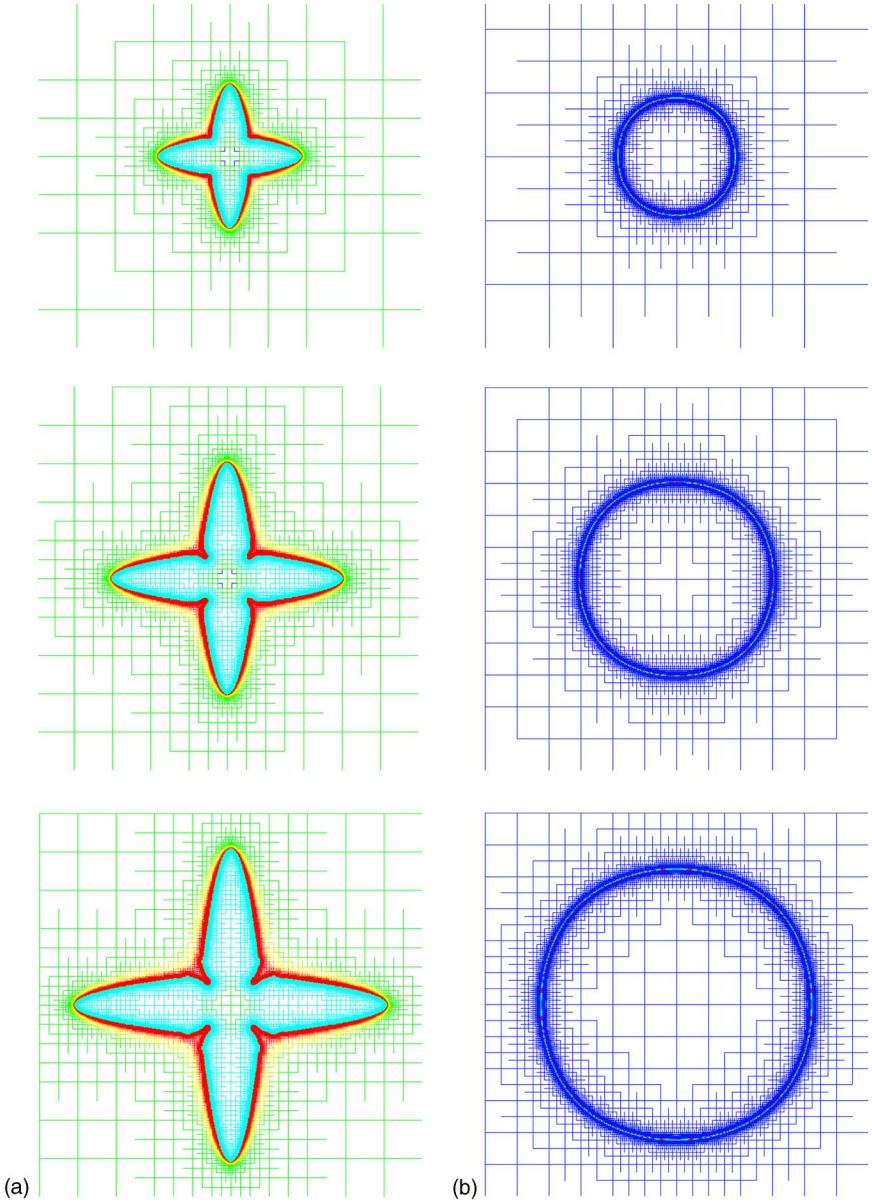

FIG. 1. (Color online) (a) Concentration map of equiaxed dendrite structure obtained at dimensionless supersaturation $\Omega=0.73$. The system size shown is $1000w \times 1000w$ and the configurations (from left to right) were taken at $t=1800\tau$, 3800τ, and 5800τ, respectively. (b) Concentration map of uniform crystal morphology obtained at a higher supersaturation $\Omega=0.85$. The system size shown is $1200w \times 1200w$ and the configurations (from left to right) were taken at $t=225\tau$, 375τ, and $t=525\tau$, respectively. Warm colors denote high concentration and cold colors represent low concentration.

IV. SOLIDIFICATION GROWTH RATE SELECTION

Figure 2 shows dendrite tip speeds extracted from our simulations versus undercooling for $l_A^{\text{eff}}/l_A=5,10,20,40$, and 100. For all cases, velocity undergoes a continuous transition between a low-velocity and a high-velocity branch at a critical temperature, denoted here as T_c. As a comparison, the inset of Fig. 2 also compares the dendrite tip velocity below the transition temperature to the tip velocity predicted by simulating the thin-interface limit of the dilute binary alloy model of Ref. [20], which uses an antitrapping term to correct for solute trapped by the presence of a finite interface width. The use of antitrapping ensures that the dilute binary alloy model is emulating the standard sharp-interface model where the interface is in local equilibrium.

Since we are in the dilute limit, we expect our low-undercooling results to approach those of the thin-interface limit with antitrapping. At low undercooling, our simulations with $l_A^{\text{eff}}/l_A=5$ and 100 overestimate the standard sharp-interface results. This is due to the fact that in the limit of low undercooling, it is difficult to achieve the simulation times required to reach steady state. Nevertheless, it is evident that as l_A^{eff} decreases, our simulations at low undercooling begin to converge toward the equilibrium sharp-interface limit. It should be emphasized that the precise convergence at low undercooling is not of specific importance here, as our focus is on the solidification kinetics in the high-undercooling regime.

As undercooling increases, we expect solute trapping to become important as the solute diffusion length becomes of the same order as the interface width. In this limit, solidification should become kinetically limited. This is consistent with our simulations in the main part of Fig. 2, which show a sharp rise in the velocity at a critical temperature. The transition in the velocity occurs when $v \sim D_L^{\text{eff}}/l_A^{\text{eff}}$. The value of the critical temperature and velocity jump at the transition were estimated by extrapolating our results to the limit $l_A^{\text{eff}} \rightarrow l_A$. Specifically, we found that $T_c \approx 1701$ K.

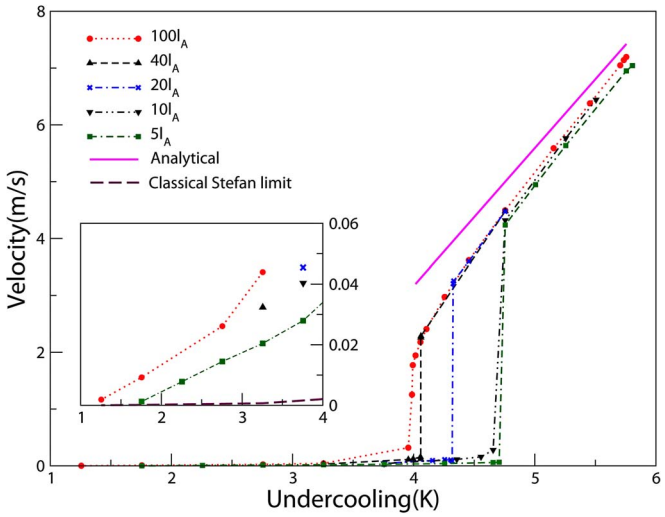

FIG. 2. (Color online) Growth rate versus undercooling for different interface widths and solute diffusion coefficient. The inset is an enlargement of the low-undercooling portion of main figure. The "Analytical" data set refers to the solute trapping model of Aziz and co-workers discussed in Ref. [23].

To further check the consistency of our simulations, we compared our high undercooling simulation results to the 1D steady-state analysis of Ref. [23] (done in the limit where $D_L = D_S$ and $k_e < 1$), which relates the interface temperature to the local interface velocity at high undercooling according to

$$T_{\text{int}} = T_0 - \frac{v}{\tilde{\mu}_A} + \frac{24}{35}\frac{v_D}{v} m_L(v) C_\infty \ln(1/k_e) \tag{8}$$

where

$$T_0 = T_M^A + m_L^e C_\infty \frac{\ln(1/k_e)}{1 - k_e}, \tag{9}$$

$$v_D \approx 0.207 \frac{D_L}{l_A} \frac{\ln(1/k_e)}{(1 - k_e)}, \tag{10}$$

where T_{int} is the temperature at the interface, v is the interface velocity, $m_L(v)$ is the velocity-dependent liquidus slope [16,23], evaluated in the limit of small C_∞. The straight line denoted "Analytical" in Fig. 2 corresponds to the large-v limit of Eq. (8), and shows that at high undercooling, our simulations approach the continuous-growth model prediction (e.g., Refs. [16,23]) for all l_A used (note that we neglected curvature and set $C_S \approx C_\infty$ and the real partition coefficient $k \approx 1$).

We note that the value of the kinetic coefficient employed in this work is considerably larger than that reported in other work [35,36]. A smaller kinetic coefficient will generate a small plateau in the velocity vs undercooling curve just prior to undergoing the transition [17,18] to the linear behavior of Eq. (8), which we also expect to observe in our phase-field simulations.

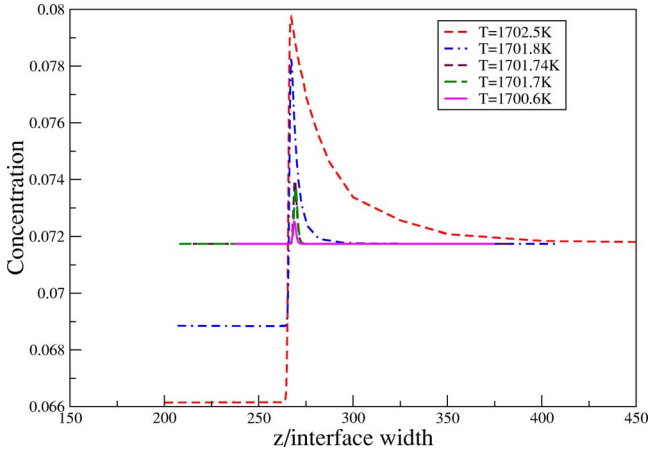

FIG. 3. (Color online) Concentration versus position obtained at different undercoolings. The data have been shifted so that the interface positions line up.

Our velocity vs undercooling data are consistent with experimental data for a Ni-0.007B alloy in Ref. [10], exhibiting both the existence of a velocity jump to a high-v branch, as well as an approach toward a linear growth rate above the transition.This transition in growth rate is also consistent with a semiempirical model presented in Ref. [10], which incorporates Aziz and co-workers' velocity-dependent solute partitioning function (see below). It is also consistent with a marginal stability analysis of a nonequilibrium sharp-interface solidification model in Refs. [17,18], which assumes a crossover from partial to complete solute trapping beyond a critical velocity, after which the growth is thermally controlled. Our phase-field simulations and previous sharp-interface analyses suggest that as solute trapping effects become large enough, interface kinetics will start to dominate the growth process, leading to a transition in growth velocity toward a linear dependence on undercooling. A more quantitative treatment of solidification at high undercooling must incorporate heat transfer into our existing equations. Phase field simulations investigating the role of solute transport vs heat transfer in this transition will be presented in future publications.

V. NONEQUILIBRIUM SOLUTE PARTITIONING

Figure 3 plots five steady-state concentration profiles near the interface region for five different temperatures for the case $l_A^{\text{eff}} = 100 l_A$. It can be seen that the diffusion length is decreasing with undercooling, with the concentration profile becoming essentially a spike at the interface as $T \approx T_c$. Above T_c, $C_S/C_L \approx k_e = C_S^{\text{eq}}/C_L^{\text{eq}}$. For $T < T_c$, on the other hand, $C_S/C_L \to 1$.

Figure 4 plots the interface values of C_S and C_L (for the case where $l_A^{\text{eff}} = 100 l_A$) versus undercooling. The value of C_S was obtained by examining the solute concentration far away from the interface in the solid phase, while C_L was identified with the maximum value of C in the interfacial region. Figure 4 also shows the equilibrium solid-liquid concentrations vs. undercooling (indicted by the straight liquidus and soli-

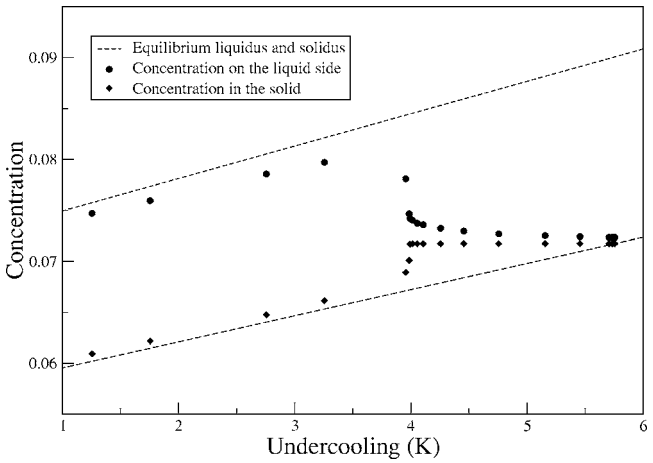

FIG. 4. Simulated interface concentrations versus undercooling. The equilibrium values are also shown for comparison by the dashed lines. The systematic shift of our simulation from the equilibrium values at low undercooling is due to curvature.

dus lines). This behavior of the solute concentration is also directly analogous to that reported by Eckler *et al.* [10]. The rise of solute concentration in the solid phase above its equilibrium value and toward the initial liquid concentration indicates a reduced amount of solute rejected away from the solid. This limit is indicated in a smooth transition in the solute partition coefficient, which we found to follow almost perfectly the expression of Aziz and co-workers [16,23] given by

$$k(v) = \frac{k_e + v/v_D}{1 + v/v_D}. \tag{11}$$

The nonequilibrium partition coefficient exhibits a smooth transition as $v \sim v_D$, which according to Eq. (10) also occurs when the solute diffusion length approaches $D_L/v \sim l_A$.

VI. CONCLUSIONS

The time-dependent growth of isothermal 2D dilute Ni -Cu alloy dendrites was simulated using a phase-field model. To make contact with the thin-interface limit at low undercooling, we used a finite-difference adaptive mesh refinement algorithm. Crystal morphologies were consistent with previous analytical and phase field simulations [31,32], exhibiting a transition from dendritic to globular patterns above the absolute stability limit. Similarly, we confirmed that solute partitioning is greatly reduced as interface velocity is increased, following the partitioning law of the continuous growth model of Aziz and Kaplan [15], and consistent with other sharp-interface models [37].

The main focus of our work was the examination of self-consistent velocity selection from low to high undercooling. At low undercooling (and as the interface width approached its true nanoscale value), dendritic growth velocity was found to approach the thin-interface predictions of the dilute binary alloy phase field model of Karma [20]. In the thin-interface limit of this phase-field model, interface properties are essentially in local equilibrium, with negligible interface kinetics. At high undercooling our phase simulations exhibit the characteristic transition to a kinetically driven growth velocity, a situation predicted by the continuous growth model of Aziz and Kaplan [15], a 1D steady-state analysis of Ahmad *et al.* [23] and a marginal stability analysis of a non-equilibrium sharp interface model of Galenko and Danilov [18]. Our simulations demonstrate that *dynamical* phase-field models of solidification, by virtue of a nonzero interface width, and depending on the length and time scales over which solute partitioning must occur, are able to capture the correct phenomenology of equilibrium and nonequilibrium dendritic growth kinetics over a wide range of undercooling. Further work is currently under way to extend our phase-field model to include the competition between mass and heat transport effects. It is noteworthy that our results are not expected to be specific to the phase-field model we simulated, as they arise from solute trapping due to the competition between two length scales, namely, the solute diffusion length and the interface thickness. Furthermore, while our simulations were carried out for a two-dimensional system, the transition should take place for three-dimensional solidification structures as well.

We believe our simulations may also offer an explanation for the observations of Ref. [7], which examine the role of interface kinetic anisotropy in the transition from dendritic to dense-branched crystal morphology. This work showed that the addition of kinetic anisotropy—determined quantitatively from careful molecular dynamics simulations—was not sufficient to predict (1) the experimentally observed dendrite to dense-branched transition in pure nickel, or (2) a shift in the dendrite velocity at high undercooling. The authors speculated that a possible reason is that the experimental samples they compared their simulations to may not in fact be "pure" nickel, but may contain trace impurities, i.e., be a binary alloy, requiring in fact a model similar to that studied in this work.

As a final note, thermal instabilities may also affect the morphology of the solidification front when the thermal diffusion length α/v becomes comparable to the scale of the growing crystal. This occurs in both the limits of large crystal sizes and low growth velocities and small crystal sizes and high growth velocities. Nevertheless, there is a window in which the crystal size is too small to be affected by the thermal instability and thus spherical morphologies occur above the critical undercooling. We are currently examining this interplay between solute and thermal instabilities, and will report on this investigation in the future.

ACKNOWLEDGMENTS

This work has been in part supported by the National Science and Engineering Research Council of Canada (N.P.) and NSF-DMR Grant No. 0449184 (M.H.).

[1] D. A. Kessler, J. Koplik, and H. Levine, Phys. Rev. A **31**, 1712 (1985).
[2] E. Ben-Jacob, N. Goldenfeld, B. G. Kotliar, and J. S. Langer, Phys. Rev. Lett. **53**, 2110 (1984).
[3] J. S. Langer, *Directions in Condensed Matter Physics* (World Scientific, Singapore, 1986), p. 164.
[4] D. A. Kessler, J. Koplik, and H. Levine, Phys. Rev. A **30**, 3161 (1984).
[5] A. Karma and W.-J. Rappel, Phys. Rev. E **53**, R3017 (1996).
[6] N. Provatas, N. Goldenfeld, and J. Dantzig, Phys. Rev. Lett. **80**, 3308 (1998).
[7] J. Bragard, A. Karma, Y. H. Lee, and M. Plapp, Interface Sci. **10**, 121 (2002).
[8] M. C. Fleming and Y. Shiohara, Mater. Sci. Eng., A **178**, 129 (1994).
[9] R. Willnecker, D. M. Herlach, and B. Feuerbacher, Phys. Rev. Lett. **62**, 2707 (1989).
[10] K. Eckler, R. F. Cochrane, D. M. Herlach, B. Feuerbacher, and M. Jurisch, Phys. Rev. B **45**, 5019 (1992).
[11] C. B. Arnold, M. J. Aziz, M. Schwarz, and D. M. Herlach, Phys. Rev. B **59**, 334 (1999).
[12] J. C. Baker and J. W. Cahn, Acta Metall. **17**, 575 (1969).
[13] J. C. Baker and J. W. Cahn, *Solidification* (ASM, Metals Park, OH, 1971), p. 23.
[14] M. Hillert and B. Sundman, Acta Metall. **24**, 731 (1976).
[15] M. J. Aziz and T. Kaplan, Acta Metall. **36**, 2335 (1988).
[16] M. J. Aziz and W. J. Boettinger, Acta Metall. Mater. **42**, 257 (1994).
[17] P. K. Galenko and D. A. Danilov, Phys. Lett. A **235**, 271 (1997).
[18] P. K. Galenko and D. A. Danilov, J. Cryst. Growth **197**, 992 (1999).
[19] P. R. Algoso, W. H. Hofmeister, and R. J. Bayuzick, Acta Mater. **51**, 4307 (2003).
[20] A. Karma, Phys. Rev. Lett. **87**, 115701 (2001).
[21] B. Echebarria, R. Folch, A. Karma, and M. Plapp, Phys. Rev. E **70**, 061604 (2004).
[22] N. Provatas, M. Greenwood, B. Athreya, N. Goldenfeld, and J. Dantzig, Int. J. Mod. Phys. B **19**, 4525 (2005).
[23] N. A. Ahmad, A. A. Wheeler, W. J. Boettinger, and G. B. McFadden, Phys. Rev. E **58**, 3436 (1998).
[24] N. Goldenfeld, B. P. Athreya, and J. A. Dantzig, Phys. Rev. E **72**, 020601(R) (2005).
[25] N. Provatas, N. Goldenfeld, J. Dantzig, J. C. Lacombe, A. Lupulescu, M. B. Koss, and M. E. Glicksman, Phys. Rev. Lett. **82**, 4496 (1999).
[26] K. R. Elder, M. Katakowski, M. Haataja, and M. Grant, Phys. Rev. Lett. **88**, 245701 (2002).
[27] K. Elder, J. Barry, and N. Provatas, TMS Lett. **3**, 41 (2004).
[28] R. Willnecker, Y. C. Chang, and C. J. Shih, Acta Mater. **51**, 1857 (2003).
[29] W. J. Boettinger, R. J. Schaefer, F. S. Biancaniello, and D. Shechtman, Metall. Trans. A **15**, 55 (1984).
[30] A. Ludwig and W. Kurz, Acta Mater. **44**, 3643 (1996).
[31] W. J. Boettinger and J. A. Warren, J. Cryst. Growth **200**, 583 (1999).
[32] D. Danilov and B. Nestler, Phys. Rev. Lett. **93**, 215501 (2004).
[33] W. W. Mullins and R. F. Sekerka, J. Appl. Phys. **34**, 323 (1963).
[34] J. C. Ramirez, C. Beckermann, A. Karma, and H. J. Diepers, Phys. Rev. E **69**, 051607 (2004).
[35] J. J. Hoyt, B. Sadigh, M. Asta, and S. M. Foiles, Acta Mater. **47**, 3181 (1999).
[36] J. J. Hoyt, M. Asta, and A. Karma, Mater. Sci. Eng., R. **41**, 121 (2003).
[37] S. L. Sobolev, Phys. Status Solidi A **156**, 293 (1996).